

Impact of proton irradiation on conductivity and deep level defects in $\beta\text{-Ga}_2\text{O}_3$ ^{EP}

Cite as: APL Mater. **7**, 022510 (2019); <https://doi.org/10.1063/1.5054826>

Submitted: 04 September 2018 . Accepted: 10 October 2018 . Published Online: 14 December 2018

M. E. Ingebrigtsen ^{id}, A. Yu. Kuznetsov, B. G. Svensson, G. Alfieri, A. Mihaila, U. Badstübner, A. Perron, L. Vines, and J. B. Varley

COLLECTIONS

Paper published as part of the special topic on [Wide Bandgap Oxides](#)

EP This paper was selected as an Editor's Pick



View Online



Export Citation



CrossMark

ARTICLES YOU MAY BE INTERESTED IN

[Impact of deep level defects induced by high energy neutron radiation in \$\beta\text{-Ga}_2\text{O}_3\$](#)

APL Materials **7**, 022502 (2019); <https://doi.org/10.1063/1.5054606>

[Deep acceptors and their diffusion in \$\text{Ga}_2\text{O}_3\$](#)

APL Materials **7**, 022519 (2019); <https://doi.org/10.1063/1.5063807>

[A review of \$\text{Ga}_2\text{O}_3\$ materials, processing, and devices](#)

Applied Physics Reviews **5**, 011301 (2018); <https://doi.org/10.1063/1.5006941>

additive manufacturing epitaxial crystal growth cerium oxide polishing powder silver nanoparticles sputtering targets III-IV semiconductors CVD precursors europium phosphors

deposition slugs OLED Lighting spintronics solar energy

GDC Li-ion battery electrolytes 99.999% ruthenium spheres

endoheral fullerenes copper nanoparticles diamond micropowder

CIGS MBE grade materials palladium catalysts flexible electronics

beta-barium borate borosilicate glass dysprosium pellets YBCO

pyrolytic graphite 3d graphene foam indium tin oxide mesoporous silica

raman substrates sapphire windows tungsten carbide InGaAs

barium fluoride carbon nanotubes lithium niobate scandium powder

gallium lump glassy carbon nanodispersions InAs wafers laser crystals ultra high purity materials MOFs

surface functionalized nanoparticles organometallics quantum dot rare earth metals photovoltaics refractory metals MOCVD

superconductors transparent ceramics ultra high purity silicon

*American Elements opens up a world of possibilities so you can **Now Invent!***

Over 15,000 certified high purity laboratory chemicals, metals, & advanced materials and a state-of-the-art Research Center. Printable GHS-compliant Safety Data Sheets. Thousands of new products. And much more. All on a secure multi-language "Mobile Responsive" platform.

perovskite crystals yttrium iron garnet alternative energy h-BN

gold nanocubes graphene oxide macromolecules photonics

rhodium sponge fiber optics beamsplitters infrared dyes zeolites

fused quartz metallocenes platinum ink buckyballs Ti-6Al-4V

Now Invent.™
The Next Generation of Material Science Catalogs

www.americanelements.com



Impact of proton irradiation on conductivity and deep level defects in β -Ga₂O₃

Cite as: APL Mater. 7, 022510 (2019); doi: 10.1063/1.5054826
Submitted: 4 September 2018 • Accepted: 10 October 2018 •
Published Online: 14 December 2018



M. E. Ingebrigtsen,¹  A. Yu. Kuznetsov,¹ B. G. Svensson,¹ G. Alfieri,² A. Mihaila,² U. Badstübner,²
A. Perron,³ L. Vines,¹ and J. B. Varley³

AFFILIATIONS

¹Department of Physics/Centre for Materials Science and Nanotechnology, University of Oslo, P.O. Box 1048, Blindern, N-0316 Oslo, Norway

²ABB Corporate Research, Segelhofstrasse 1K, 5405 Baden-Dättwil, Switzerland

³Lawrence Livermore National Laboratory, Livermore, California 94550, USA

ABSTRACT

Single crystalline bulk and epitaxially grown gallium oxide (β -Ga₂O₃) was irradiated by 0.6 and 1.9 MeV protons to doses ranging from 5×10^9 to 6×10^{14} cm⁻² in order to study the impact on charge carrier concentration and electrically active defects. Samples irradiated to doses at or above 2×10^{13} cm⁻² showed a complete removal of free charge carriers in their as-irradiated state, whereas little or no influence was observed below doses of 6×10^{12} cm⁻². From measurements at elevated temperatures, a thermally activated recovery process is seen for the charge carriers, where the activation energy for recovery follows a second-order kinetics with an activation energy of ~ 1.2 eV. Combining the experimental results with hybrid functional calculations, we propose that the charge carrier removal can be explained by Fermi-level pinning far from the conduction band minimum (CBM) due to gallium interstitials (Ga_i), vacancies (V_{Ga}), and antisites (Ga_O), while migration and subsequent passivation of V_{Ga} via hydrogen-derived or V_O defects may be responsible for the recovery. Following the recovery, deep level transient spectroscopy (DLTS) reveals generation of two deep levels, with energy positions around 0.75 and 1.4 eV below the CBM. Of these two levels, the latter is observed to disappear after the initial DLTS measurements, while the concentration of the former increases. We discuss candidate possibilities and suggest that the origins of these levels are more likely due to a defect complex than an isolated point defect.

© 2018 Author(s). All article content, except where otherwise noted, is licensed under a Creative Commons Attribution (CC BY) license (<http://creativecommons.org/licenses/by/4.0/>). <https://doi.org/10.1063/1.5054826>

Gallium oxide (Ga₂O₃) is a wide bandgap semiconductor ($E_g \sim 4.8$ eV^{1,2}), which has received considerable attention during the past years due to its potential applications in UV detectors and high-voltage devices.³ The most stable phase at ambient conditions, β -Ga₂O₃, has a high breakdown field, estimated at ~ 8 MV/cm,⁴ which is a major advantage in power electronics. However, the technological advances of Ga₂O₃ are hampered by the difficulty in controlling and understanding the electrical behavior of intrinsic and impurity-related defects. Similar to most other oxide semiconductors, β -Ga₂O₃ shows inherent *n*-type conductivity, where native defects may play an important role. Several of the primary defects are electrically active, where hybrid functional calculations have suggested gallium vacancies (V_{Ga}), as well as their complexes

with hydrogen to be deep acceptors and the gallium interstitial to be a shallow donor. The oxygen vacancy and interstitial are proposed to be deep donors and hence electrically neutral for Fermi-level positions close to conduction band minimum (CBM).^{5,6} Furthermore, the primary defects are predicted to be mobile at relatively modest temperatures; recent theoretical estimates suggest that the activation barrier for vacancy migration is in the range of 0.5–1.6 eV, while that for the gallium interstitial (Ga_i) may be as low as 0.1 eV.^{7,8} Thus, vacancy and interstitial-related complexes may also play a crucial role for the electrical properties of β -Ga₂O₃.

So far, studies using deep level transient spectroscopy (DLTS) and deep level optical spectroscopy (DLOS) have

revealed several bandgap states,^{9–13} where both intrinsic and extrinsic origins have been proposed, although firm identification remains largely unresolved. In this respect, studying irradiated (or implanted) samples is indispensable for the identification and understanding of electrically active defects, and combined with characterization techniques like DLTS, it is a powerful concept to obtain insight into their origin and formation kinetics. Herein, we report on the consequences of subjecting bulk and epitaxial β -Ga₂O₃ samples to 0.6 and 1.9 MeV proton irradiation. We first describe how a loss of charge carriers is observed during irradiation, with a subsequent recovery during DLTS scans up to 650 K. We then assess the irradiation-induced deep level defects using a combination of DLTS measurements and hybrid functional calculations and discuss their possible origins for the carrier depletion and recovery based on the results.

For the experimental measurements, we studied bulk single crystals and homoepitaxial β -Ga₂O₃ films synthesized by Tamura Corporation. The bulk crystals were grown by Edge-defined Film-fed Growth (EFG) and cut with a (010) surface orientation. These wafers were nominally undoped but exhibited *n*-type conductivity with charge carrier concentrations (N_d) in the range of 0.7 – $2.3 \times 10^{17} \text{ cm}^{-3}$. The homoepitaxial films were grown on (001) and (010) oriented substrates by hydride vapor phase epitaxy (HVPE) and molecular beam epitaxy (MBE), respectively. While the substrates for the films were Sn-doped to $N_d \sim 5 \times 10^{18} \text{ cm}^{-3}$, the $10\text{-}\mu\text{m}$ -thick HVPE films and the $2\text{-}\mu\text{m}$ -thick MBE films showed $N_d \sim 8 \times 10^{16} \text{ cm}^{-3}$ and $\sim 3 \times 10^{16} \text{ cm}^{-3}$, respectively. Samples cut from the bulk single crystals will hereafter be referred to as bulk samples, while the epitaxially grown are labeled HVPE and MBE in accordance with their synthesis method.

For the electrical characterization, Schottky contacts were deposited through a shadow mask using e-beam evaporation of 150 nm Ni, yielding circular contacts of radii 100, 240, and 400 μm . Furthermore, backside Ohmic contacts were prepared by e-beam deposition of a Ti and Al stack of 10 and 150 nm thicknesses, respectively. Barrier heights of the Schottky contacts as high as $\sim 1.4 \text{ eV}$ and ideality factors as low as 1.05 were found from current-voltage characteristics with up to eight orders of magnitude rectification.¹¹

After preparation and initial characterization, the samples were implanted at room temperature in vacuum ($< 5 \times 10^{-7} \text{ Torr}$), with H⁺ ions to study the generation of damage. High acceleration potentials were chosen to place the implantation peaks far from the depletion region in order to not observe the ions themselves but to study the generation of intrinsic secondary defects. Hence, the damage from implantation is irradiation-like, with flat damage profiles in the tail region probed by capacitance measurements close to the surface. For the H⁺ ions, two ion energies were chosen. First, low doses in the range of 5×10^9 to $5 \times 10^{10} \text{ cm}^{-2}$ were prepared with 1900 keV H⁺ ions, having a projected range of 22 μm , as estimated by simulations using the SRIM code.¹⁴ Second, samples were implanted using 600 keV H⁺ ions with doses ranging from 6×10^{11} to $6 \times 10^{14} \text{ cm}^{-2}$ and a projected range (R_p) of

$\sim 4.3 \mu\text{m}$. DLTS was carried out while scanning up and down in temperature using a refined version of a setup described in Ref. 15, and a quiescent reverse bias of -8 V was used along with filling pulses to -1 V bias for 50 ms duration. A temperature range up to 650 K was employed to probe levels deep into the bandgap, and the measurements were carried out in a chamber evacuated to a rough vacuum ($\leq 10^{-3} \text{ Torr}$).

To evaluate the energetics of various native defects and complexes that may contribute to the DLTS signals, we performed calculations using the Heyd-Scuseria-Ernzerhof (HSE06) screened hybrid functional¹⁶ and projector-augmented wave (PAW) approach¹⁷ as implemented in the VASP code.¹⁸ We include semi-core Ga 3*d* electrons as explicit valence states and set the fraction of screened Hartree-Fock exchange to 32% which accurately describes both the experimental bandgap and the structural parameters as reported elsewhere.^{2,19} Owing to the complexity and size of various vacancy complexes, we adopted 160-atom supercells as evaluated with a plane wave cutoff of 400 eV and a single shifted Monkhorst-Pack *k*-point at 0.25, 0.25, 0.25. We assess the point defect formation energies and their associated electronic transition levels using the formalism as described previously, with finite-size corrections adopted using the schemes in Refs. 20–22. To additionally assess the uncertainty in our reported defect levels, we consider the two extremes where the charged defects are corrected using the experimental dielectric constants that reflect the purely electronic contribution (ϵ_∞) and additionally including ionic screening contributions owing to the response of the lattice to the defect (ϵ_0).^{19,23} In principle, the ϵ_0 should be used, but owing to the large size of the defects and complexes considered in our relatively small, periodically repeated supercell, there may not be appropriate screening to fully capture the ϵ_0 in this highly polar and anisotropic material.⁶ Convergence tests for the $V_{\text{Ga}^{-3}}$ suggest that ϵ_0 is still a far better choice than ϵ_∞ , which we find yields inadequately-corrected values that still suffer from a significant supercell-size dependence (see [supplementary material](#)). Nonetheless, we consider both limits to provide more transparency in possible uncertainty of theoretically reported levels and to assist in resolving the identification of the defect states experimentally identified in Ga₂O₃. Further experimental evidence will help clarify the limitations in the current theoretical approaches and identify which model of the screening is most appropriate for making reliable predictions. In the manuscript, we include plots using the ϵ_0 data, whereas plots using ϵ_∞ and additional details of the calculations are provided in the [supplementary material](#).

Samples that were subjected to H⁺ doses at or above $2 \times 10^{13} \text{ cm}^{-2}$ exhibited a near-complete removal of charge carriers in the depletion region, as manifested through a reduction in the measured capacitance. In these samples, the remaining capacitance is in the order of a few pF and in reasonable agreement with a depletion depth that corresponds to the implanted peak depth (projected range, R_p). Furthermore, the capacitance does not respond to the voltage changes of our measurements. From this it seems that instead of probing the region near the Schottky contact, in the range of

50–500 nm as is typical for the un-irradiated samples, the capacitance of as-irradiated samples is defined by the implantation peak. Contrarily, at lower doses, below $6 \times 10^{12} \text{ cm}^{-2}$, similar capacitance reduction is not observed.

SRIM simulations using a threshold energy for displacement of atoms of 15 eV, a typical value for semiconductors,^{24,25} estimate the vacancy generation from 600 keV H^+ ions to be 1.1×10^{-5} vacancies/(ion Å) [$\#/(ion \text{ \AA})$] in the tail region of the implantation. The corresponding peak value around the projected range of the ions was $\sim 3.9 \times 10^{-3} \#/(ion \text{ \AA})$. Of the generated defects, consider 5% a generous upper limit for the amount that survives dynamic annealing. Thus, for a dose of $2 \times 10^{13} \text{ cm}^{-2}$, this results in an upper limit of the defect concentrations of 1.1×10^{16} and $3.9 \times 10^{17} \text{ cm}^{-3}$ for the tail region and around R_p , respectively. With carrier concentrations in the range of 10^{16} – 10^{17} cm^{-3} , the estimated defect generation in the implantation tail is insufficient to account for the charge carrier removal. Hence, this corroborates that the removal is likely to occur due to the region around R_p . Nonetheless, the removal occurring in the region around R_p indicates a low dynamic annealing of the irradiation-induced defects, in accordance with that observed for low-temperature irradiations using ohmic contacts.²⁶ In addition, it indicates a substantial formation of electrically active intrinsic defects in the samples.

Annealing the irradiated samples at temperatures above 450–650 K results in the recovery of charge carriers in a thermally stimulated process. Figure 1 shows the recovery of the reverse bias capacitance as a function of temperature from DLTS measurements on as-irradiated samples of HVPE and bulk material. For ease of comparison, the capacitance was normalized to the value at room temperature before irradiation. The solid symbols show the measurements during

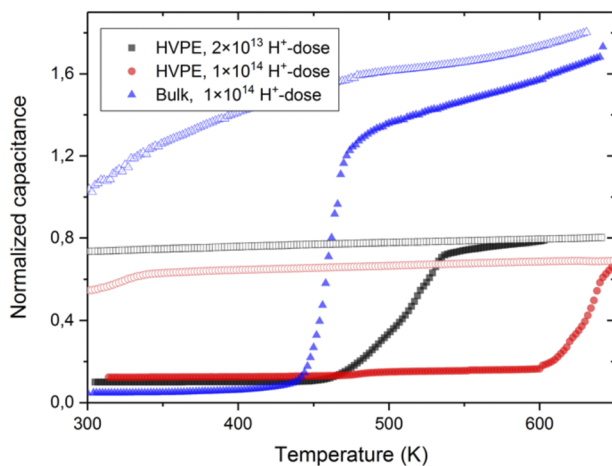


FIG. 1. Recovery of the reverse bias capacitance during DLTS measurements on irradiated samples, normalized to the capacitance before irradiation. The recovery gives a distinctive step in capacitance during heating (solid symbols) and the recovered charge carriers remain during cooling (open symbols). The temperature position of the step seems dependent on both irradiation dose and sample type.

heating and the open symbols display the measurement during the subsequent cooling, where the cooling/heating was carried out at a rate of 2 K/min. Distinctive steps in the capacitance are seen in the measurements when heating the samples from their as-irradiated state, representing recovery of charge carriers. Interestingly, for the HVPE samples, this step appears at a lower temperature for the sample irradiated to a dose of $2 \times 10^{13} \text{ cm}^{-2}$ compared with that of $1 \times 10^{14} \text{ cm}^{-2}$, and recovery appears stronger in the bulk sample compared with that of the HVPE for a similar dose.

We will, in the following, focus our attention on this charge carrier recovery, which appears to be a thermally activated process, and study the kinetics of this reaction. Bulk samples irradiated to H^+ doses of 3×10^{14} and $6 \times 10^{14} \text{ cm}^{-2}$ were subject to continuous CV measurements at constant temperatures. Figure 2 shows the charge carrier concentration (n) as a function of depth of the bulk sample for the higher dosage as it develops over time at a constant temperature of 510 K. The values were calculated from CV measurements performed over 6 h, and warmer colors correspond to longer time. In Fig. 3, data from three depletion depths are extracted, from the same CV profiles, and presented as charge carrier concentration as a function of time. Immediately it is evident that the recovery in Fig. 2 occurred at a higher temperature and on a longer time scale than the lower dose-irradiated bulk sample in Fig. 1. This is in agreement with the dose dependence of the HVPE samples in Fig. 1, hence suggesting a dependence of the reaction rate on the initial concentration of an irradiation-induced defect. As a side note, we remark also that the recovery process is not dependent on the biasing conditions of the samples, as we see the same recovery in other diodes on the same samples that were not biased during the reported heat treatments (not shown).

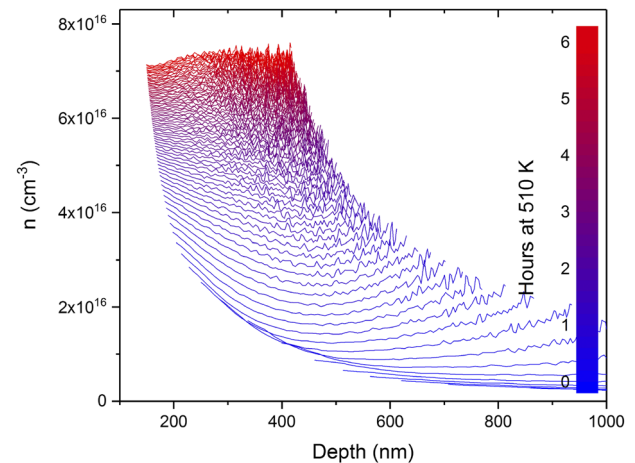


FIG. 2. Recovery of charge carrier concentration (n) with time in bulk sample irradiated with $6 \times 10^{14} \text{ cm}^{-2} \text{ H}^+$. The charge carrier concentration is presented as a function of depth during a 6-h heat treatment at 510 K, where warmer colors correspond to longer time.

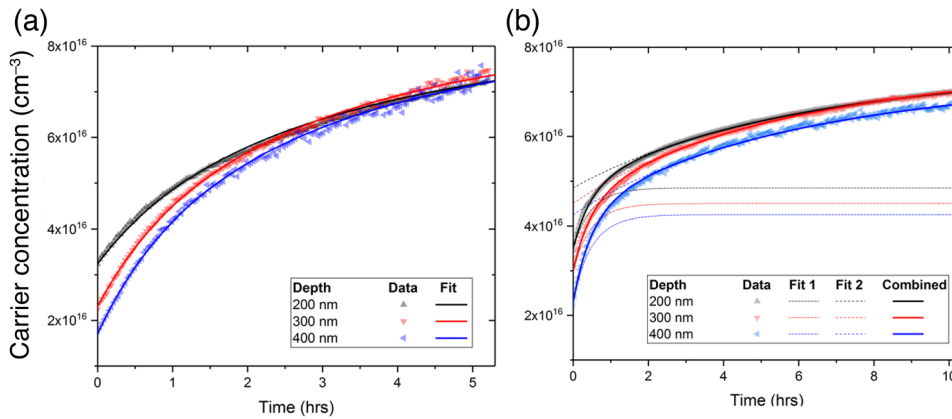


FIG. 3. The charge carrier concentration (n) at three depths shown as a function of time in the bulk sample irradiated with a dosage of (a) $6 \times 10^{14} \text{ cm}^{-2}$ and (b) $3 \times 10^{14} \text{ cm}^{-2} \text{ H}^+$. The fit in (a) indicates a reaction with second-order kinetics and activation energy of 1.2 eV, while a single second-order kinetic reaction does not sufficiently describe the reaction in (b) and is better fit with two activation energies of 1.18 and 1.28 eV.

Since the exact precursors for the reaction and the origin of the free charge carriers from the product are not known, a reaction equation cannot be directly defined. However, the time dependence can be studied and thereby the reaction kinetics. Initially, first-order kinetics was attempted to explain the reaction rate, where the rate of the reaction only depends on the concentration of a single reactant. However, first-order kinetics does not yield good fit to the experimental data (not shown) and can be discarded. This indicates that we can exclude dissociation of a center and a diffusion-limited reaction with another defect/impurity species having a concentration about one order of magnitude (or more) higher than that of the defect center itself as the dominant process. On the other hand, a good fit is achieved for second-order kinetics, as presented by the solid lines in Fig. 3(a). Interestingly, second-order kinetics can be achieved by diffusion of an irradiation-induced defect and the subsequent trapping by a defect of similar concentration following the reaction equation, $A + B = C$. Hence, the reaction rate will depend on the concentrations of both A and B,

$$\text{rate} = \frac{d[C]}{dt} = k[A][B].$$

The reaction rate constant k can further be described as $k = 4\pi RD$, where R is the capture radius and the diffusivity D is ascribed to the mobile specie. In the fit in Fig. 3(a), we assume $R = 5 \text{ \AA}$ from geometrical considerations, and using diffusivity $D = D_0 \exp(-E_a/k_B T)$, the activation energy for migration is found to be $E_a = 1.2 \text{ eV}$, given a reasonable prefactor of $D_0 = 1.88 \times 10^{-3} \text{ cm}^2 \text{ s}^{-1}$.²⁷ In addition to the dose dependence of the recovery temperature indicated in Fig. 1, it is possible to infer that the difference between bulk and HVPE samples is related to different concentrations of the second precursor of the reaction above. Indeed, the impurity content in the bulk samples has been shown to be higher than that in the HVPE samples.¹⁹

In Fig. 3(b), we discuss the same analysis for the bulk sample implanted with lower dose of $3 \times 10^{14} \text{ cm}^{-2}$. This complicates the interpretation as the recovery takes longer time at a slightly higher temperature (520 K) than in Fig. 3(a),

hence countering the dose dependence that seemed apparent above. However, it is evident that a single second-order kinetics reaction does not describe this measurement series accurately, as it increases too rapidly initially. Instead, a fit may be made considering two reactions of the kind outlined above. This implies that there may be several routes to regain charge carriers where they have been removed by irradiation-induced defects. However, both irradiation and post-irradiation annealing have been carried out under vacuum conditions; hence, adsorption and subsequent diffusion of oxygen is expected to be negligible in the present experiments.²⁸ Nonetheless, the present data indicate that migration of primary and/or impurity-related defects is important and that intrinsic and impurity-related complexes should be considered.

To gain additional insight into what defects may explain the carrier depletion and recovery behavior, we use hybrid functionals to assess the vacancies and interstitials that are expected to form via site displacement upon irradiation. We summarize the calculated formation energies in Figs. 4 and 5, and the associated charge-state transition levels are included in Table II.

As previously discussed, V_O on the different crystallographic sites are deep donors with the $\epsilon(2+/0)$ transitions falling between ~ 1.4 and 2.6 eV below the CBM for the distinct crystallographic O sites, with the shallowest levels corresponding to the four-fold coordinated O_{III} site. Oxygen interstitials (O_i) are also included in Fig. 4 and exhibit different site preferences and electronic behavior depending on the Fermi level. For example, the split-interstitial configurations (O_{si}) preferably form on the O_I site and act as deep donors that are most favorable for Fermi levels up to approximately 1 eV below the CBM. Above that, other interstitial configurations (O_i) that behave as deep acceptors become more favorable and are the preferred state in n -type conditions like that of the samples pre-irradiation and post-recovery irradiated samples.

In the event of only O-site displacement from irradiation, equivalent populations of V_O and O_i would lead to an excess of acceptors in n -type conditions that would drive the Fermi

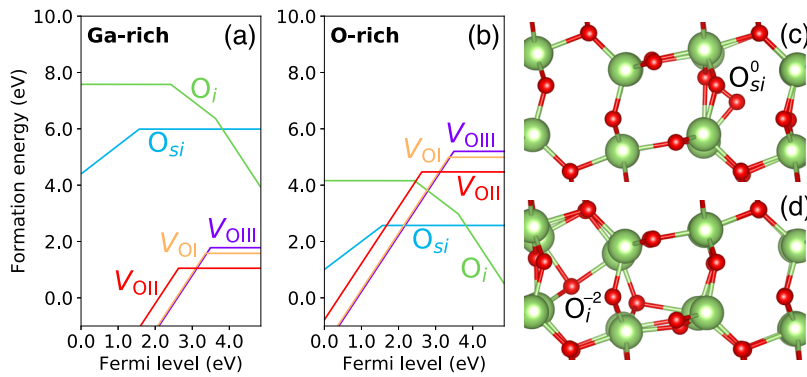


FIG. 4. Formation energy diagram of simple O-related defects expected during irradiation, shown for both Ga-rich (a) and O-rich (b) conditions. The atomic geometries associated with the favorable configurations of the O interstitial are included for (c) the neutral O_{si} and (d) the O_i^{-2} .

level away from the CBM to ensure charge neutrality. This would be satisfied by a Fermi level where the donor V_{O2}^{+2} and acceptor O_i populations balance or where neutral V_O , O_i , and O_{si} populations are the preferred charge states. From the data in Fig. 4, both these scenarios would lead to the Fermi level moving away from the CBM.

We also considered the mobility of the O_i^{-2} defects by calculating the migration barrier along the b axis for the configuration shown in Fig. 4(d) using the climbing nudged elastic band (cNEB) method and the Perdew-Burke-Ernzerhof functional revised for solids (PBEsol).^{29,30} Our results indicated a migration barrier of 0.12 eV, indicating that O_i acceptor defects are extremely mobile even below room temperature. O_i acceptors would thus likely contribute to only short-lived electrical compensation in irradiated n -type Ga_2O_3 owing to rapid diffusion away from the irradiated region or annihilation with vacant oxygen sites. They could additionally complex with other donors that may be present in the lattice and possibly form more stable centers. Remnant neutral V_O defects are considerably less mobile with predicted migration barriers of 1.7 eV for lowest energy V_{OI} migration along the b axis⁸ and would be far less likely to diffuse away from the irradiated region. Therefore, we predict that implantation energies with thresholds enough to displace O but not Ga would have a rapid

recovery of any losses in the carrier concentration owing to the rapid diffusivity of O_i compensating centers compared with neutral V_O .

For the displacement of Ga atoms, we first consider the generation of shallow donor Ga_i and deep acceptor V_{Ga} configurations in Fig. 5. We consider the lowest energy Ga_i site and possible vacancy configurations on the tetrahedral (V_{GaI}) or octahedral (V_{GaII}) Ga sites and three other configurations where two adjacent vacant Ga sites are complexed with an interstitial-like Ga, which we denote as V_{Ga}^i . Ga_i species have previously been reported to act as highly charged shallow donors (Ga_i^{+3}) that are generally unfavorable in n -type conditions⁶ and exhibit a low migration barrier in the order of 0.1 eV.⁷ We also find that Ga_i acts as a donor in n -type conditions with a high formation energy but that it exhibits additional transition levels within the bandgap that are associated with local lattice relaxations involving a neighboring Ga. Specifically, we identify a $Ga_i \epsilon(3+/+)$ transition occurring at least 0.6 eV below the CBM and above 1.46 eV below the CBM in the limit that the ionic screening is inadequately captured within our supercell. The V_{Ga}^i configurations have previously been discussed to be the most energetically favorable, exhibiting low energy barriers for formation from the respective V_{GaI} and V_{GaII} , and are believed to be the most relevant configurations, particularly in the case of n -type

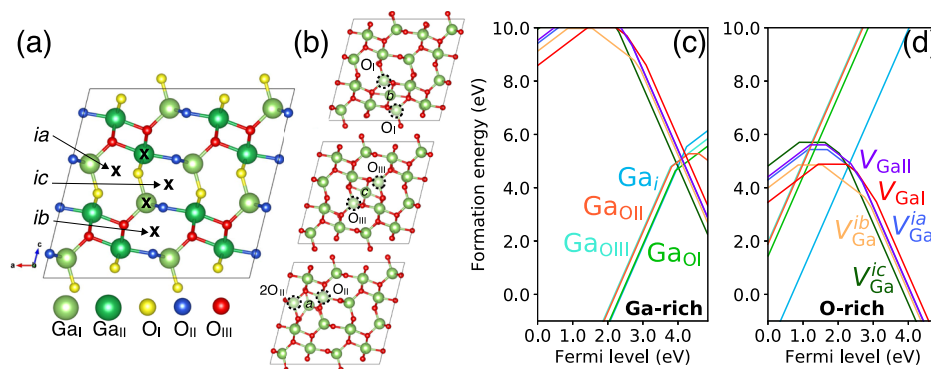


FIG. 5. Illustration of the β - Ga_2O_3 structure with the possible Ga vacancy sites highlighted (a), where three interstitial-vacancy complexes (V_{Ga}^i) are shown in (b) and denoted as V_{Ga}^{iib} , V_{Ga}^{ic} , and V_{Ga}^{ia} from top to bottom. The vacant Ga sites adjacent to the displaced interstitial Ga in (b) are highlighted with dashed circles and we also list which O species are left with dangling bonds for each vacancy configuration. Formation energy diagram of these V_{Ga} configurations and the most favorable Ga_i are shown for both Ga-rich (c) and O-rich (d) conditions.

conditions.^{8,31} All configurations are predicted to be deep acceptors, while the predicted transition levels are quite sensitive to the choice of dielectric screening used to correct for image-charge interactions.^{6,8,31,32} Of most importance to n -type samples are the ϵ ($-2/-3$) levels, which are summarized in Table II and have a reported range spanning ~ 0.7 - 2.5 eV below the CBM.

From the behavior of the Ga_i and V_{Ga} in Figs. 5(c) and 5(d), it is clear that the Fermi level associated with an equal population of these donors and deep acceptors is deep within the bandgap (roughly equivalent to where their formation energies cross). For example, this is ~ 0.8 to 2.8 eV below the CBM in Fig. 5 depending on the conditions. This supports that Ga displacement upon irradiation of n -type samples would move the Fermi level away from the CBM and facilitate a carrier depletion effect. To assess the kinetics of these defects, we again calculated the migration barrier using the PBEsol functional for the interstitial, finding a value of 0.74 eV for the Ga_i^+ for motion along the b axis. Evaluating the results with HSE led to a slightly higher value of 0.94 eV, illustrating that kinetic barriers calculated with semilocal functionals like Perdew-Burke-Ernzerhof (PBE) tend to be underestimated.³³ While we did not exhaustively consider migration along other axes or via kick-out mechanisms, these results strongly suggest that Ga_i is far less mobile than originally reported by Blanco *et al.*⁷ and less mobile than O_i acceptor species. This barrier is still modest and Ga_i donors would also be expected to rapidly diffuse out of the irradiated region or annihilate with V_{Ga} acceptors at temperature ~ 400 K which would be probed during the heat treatments. The degree with which Ga_i recombines with V_{Ga} versus diffusion away from the implantation region (leaving an excess of V_{Ga}) likely is a key factor in the dynamics of the carrier recovery and may account for the deviations in behavior observed in the capacitance in Fig. 1.

An additional possibility is the capture of mobile Ga_i donors at remnant V_{O} sites, forming Ga_{O} antisites. This is also illustrated in Fig. 5(c), where we find that the various Ga_{O} species are donors that exhibit behavior quite similar to the Ga_i , exhibiting high formation energies in n -type conditions; their transition levels are summarized in Table II. We find that the Ga_{OII} is the most favorable in n -type conditions where it acts as a deep donor with a $\epsilon(+/0)$ transition between 0.55 and 0.76 eV below the CBM. The Ga_{OII} is also predicted to exhibit an acceptor state that falls quite close to the CBM, approximately 0.25 - 0.06 eV below the CBM, depending on the finite-size corrections. While the Ga_{O} defects appear high in energy and are not likely to form during growth, we note that relative to isolated V_{O} and Ga_i that may be formed during irradiation, all three configurations exhibit binding energies in excess of 2 eV in n -type conditions. This suggests that irradiated samples likely have a substantial concentration of Ga_{O} . Tests to assess the stability of O_{Ga} antisites identified that they are deep acceptors and unstable relative to the formation of V_{Ga} and O_i constituents in n -type conditions, so we do not consider them further.

The most favorable $V_{\text{Ga}}^{\text{ib}}$ and $V_{\text{Ga}}^{\text{ic}}$ vacancy configurations are both formed adjacent to two V_{GaI} , with the barriers for hopping between the tetrahedral sites to be 1.0 and 1.4 eV, respectively.⁸ While these barriers may be underestimated owing to the PBE functional,^{31,33} they still suggest that Ga vacancies are plausible candidates that correspond to the ~ 1.2 eV activated kinetic processes related to the carrier recovery. Specifically, remnant V_{Ga} acceptors formed upon irradiation may diffuse to combine with other defects to form passivated centers that lead to reduced compensation and a return of the free carrier concentration. Thus, migration and subsequent trapping (passivation) of V_{Ga} is a plausible scenario, although the trapping center remains to be revealed. An alternative scenario is the passivation of ion irradiation-induced acceptors by mobile extrinsic defects. Here, only a few impurities have been found by SIMS in concentrations above the carrier concentration, where most of them, including Si, are expected to be very stable at temperatures around 500 - 600 K. However, hydrogen, carbon, and nitrogen are available during HVPE growth, and although they are below the detection limit of our SIMS of around 10^{18} cm^{-3} , they cannot be excluded as a precursor in a passivation process. An additional possibility is that the diffusion of the implanted H may also contribute to the carrier recovery through interaction with the residual vacancies, e.g., via passivation of V_{Ga} acceptors as V_{Ga} -H complexes or the conversion of neutral V_{O} to stable H_{O}^+ shallow donors.

To offer some insight into this, we evaluated the migration barriers of H_{O}^+ to come off-site to form more mobile H_i^+ species. For the most favorable H_{OI} configuration,⁵ we calculated a barrier of 1.23 eV for the H_{O} to come off-site and form an H_i^+ bound to an adjacent O_i site, again using the cNEB method with the PBEsol functional. Virtually identical barriers were found for H_{OIII} to come off and bind as an interstitial to an adjacent O_i , while the lowest barrier of 0.78 eV was identified for H_{OII} to bind as an interstitial to the nearest-neighbor O_{II} site. When evaluating this path using the hybrid functional, we obtain a higher barrier of 1.22 eV, which is required to dissociate the H_{OII} and form the H_i^+ species (with a reverse barrier of 0.6 eV). Barriers associated with H_i^+ migration have been reported to be 0.3 eV,^{5,34} indicating that once freed, H_i^+ may rapidly diffuse and interact with other defects such as V_{Ga} or other acceptors and facilitate passivation via the formation of highly stable complexes like V_{Ga} - 2H species recently observed.³⁵ We include the formation energies such complexes in Fig. 6, where we confirm that the $V_{\text{Ga}}^{\text{ib}}$ - 2H is the energetically preferred configuration, with a calculated binding energy of ≥ 3 eV for the 1st and ≥ 2.5 eV for the 2nd hydrogen to bind to the complex. The barrier associated with V_{OII} -mediated H diffusion also falls within the regime of the kinetic reaction fits of the carrier recovery in Fig. 3 and further complicates the identification of what defect(s) may be responsible for the recovery. Owing to this uncertainty, more detailed studies are required to confirm the mechanism(s) for charge carrier recovery after irradiation and the extent to which H- and V_{Ga} -related defects play a role.

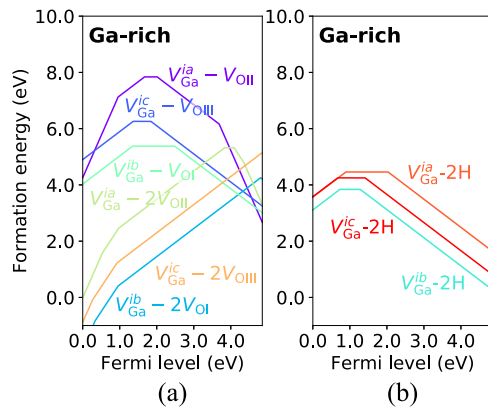


FIG. 6. Formation energy diagrams of some possible V_{Ga}^i -related complexes involving up to two V_{O} (a) and two interstitial H (b), shown for Ga-rich conditions.

Additional possibilities and complexities come from the formation of vacancy complexes like $V_{\text{Ga}} - V_{\text{O}}$. In Fig. 6, we also highlight how the combination of V_{Ga}^i configurations with V_{O} can even form stable shallow donor configurations for the V_{Ga}^{ib} and V_{Ga}^{ic} which are also likely to drive the Fermi level toward the CBM. We find that the single $V_{\text{Ga}}^i - V_{\text{O}}$ complexes effectively passivate the isolated V_{Ga}^{ib} and V_{Ga}^{ic} , reducing a -3 charge state to -1 in n -type conditions, whereas the double V_{O} -containing complexes lead to complexes that appear to act as shallow donors. Other complex configurations behave differently, where we show that the $V_{\text{Ga}}^{ia} - V_{\text{OII}}$ maintains a -3 charge state in n -type conditions, with the ϵ ($-1/-3$) transition falling closer to the CBM (see Table II). We find that the single $V_{\text{Ga}} - V_{\text{O}}$ complexes are quite stable, with binding energies of 2.5–2.8 eV for the b and c configurations, whereas the double V_{O} complexes become decreasingly stable as conditions become more n -type. For example, the more favorable $V_{\text{Ga}}^{ib} - 2V_{\text{OI}}$ complex has a binding energy of 0.4 eV at the CBM relative to isolated V_{OI} and the $V_{\text{Ga}}^{ib} - 2V_{\text{OIII}}$ complex is predicted to become unstable in these conditions. The V_{Ga}^{ia} complexes have a binding energy of 1.2 eV for the first V_{O} and 1.1 eV for the second, making them slightly more stable in n -type conditions. Considering the possible mobility of V_{O} and V_{Ga} ,⁸ the formation of such complexes may also assist in the carrier recovery via a reduction in compensation from isolated V_{Ga} .

Now, we consider the irradiation-induced deep levels through DLTS measurements. Figure 7 shows DLTS measurements of the bulk sample prior to and after irradiation of H^+ ions to a dose of $6 \times 10^{14} \text{ cm}^{-2}$. The black symbols in Fig. 5 represent a measurement before irradiation, where at least four levels are observed, which are labeled E1–E4. The levels have previously been observed in bulk material,^{9–11} with energy level positions of 0.56, 0.78, 1.01, and 1.48 eV below CBM for E1, E2, E3, and E4, respectively. Note that no DLTS peaks are observed at temperatures below 200 K. The level traditionally labeled as E2 is the most prominent one of all, and although

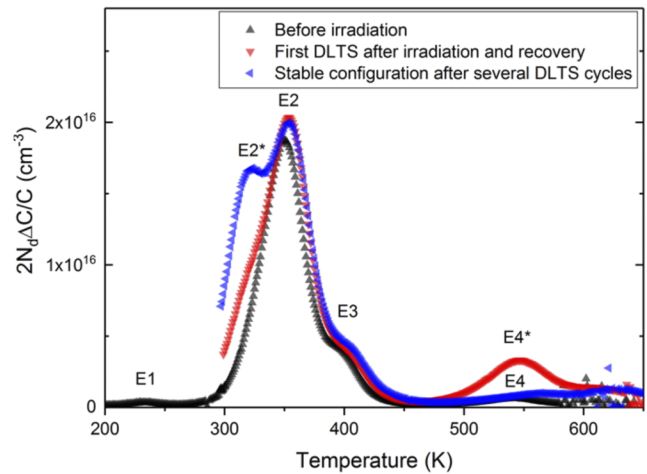


FIG. 7. DLTS measurements on bulk sample before and after irradiation with $6 \times 10^{14} \text{ cm}^{-2} \text{ H}^+$ ions. Two measurements after irradiation are presented to show the difference between the first measurement and that done after stabilization from several cycles.

the energy level position vary somewhat in the literature,^{9–11} it is particularly dominant in bulk materials. Recently, E2 was shown to be related to iron.¹⁹

The first measurement after irradiation was carried out while cooling down after heating to 650 K in the DLTS setup to recover the charge carriers as discussed above. Here, it must be emphasized that the projected range of the H^+ ions is considerably larger than that probed by the CV and DLTS measurements after the recovery. Thus, only the tail of the ion-induced defect generation profile is investigated, and we can assume a uniform defect generation profile in the dilute limit. The measurement represented by red symbols in Fig. 7 shows that the E2 concentration after irradiation is similar to that before irradiation. Meanwhile, a prominent deep level at around 550 K, labeled E4*, and a shoulder on the low temperature side of E2, labeled E2*, have emerged. During the next DLTS scan, represented by the blue symbols in Fig. 7, the E2* peak grows and the E4* peak disappears. This latter DLTS spectrum is then stable in subsequent measurements; i.e., no change in the DLTS spectrum is observed after further measurements up to 650 K. The energy positions and electron capture cross sections of the levels are summarized in Table I. It should be noted that the energy level position of E4* for the different measurements and samples varied significantly, and combined with the broad DLTS signature may indicate that the peak may consist of several overlapping levels. Furthermore, the disappearance of the level makes control measurements on the same diode challenging. This discrepancy may explain the difference compared with other reports that identify an irradiation-induced, E4-like level at 1.2 eV below the CBM.¹³ Although the observed energy position and capture cross section overlap with those previously reported for E4, a distinction in the label has been chosen to account for the behavior of the defect generated by irradiation.

TABLE I. Energy positions relative to the CBM ($E_c - E_t$) and apparent capture cross sections (σ_n) as measured via DLTS.

	E1	E2*	E2	E3	E4/E4*
$E_c - E_t$ (eV)	0.56 ± 0.03	0.75 ± 0.04	0.78 ± 0.04	1.01 ± 0.05	1.4 ± 0.15
σ_n (cm ²)	$0.3\text{-}5 \times 10^{-13}$	$3\text{-}7 \times 10^{-14}$	$0.2\text{-}1.2 \times 10^{-15}$	$2 \times 10^{-14} - 1 \times 10^{-12}$	$3 \times 10^{-15} - 2 \times 10^{-12}$

Figure 8 shows measurements on an HVPE sample prior to and after irradiation to a dose of 2×10^{13} cm⁻². The measurement before irradiation (black symbols) shows only a small E2 concentration in this sample. After irradiation, E2* and E4* appear (first measurement, red symbols), similar to those observed in the bulk samples. Moreover, the following measurements (blue symbols) show a similar decrease in E4* as in Fig. 7, and also an increase in E2*. It should be pointed out that the samples remain *n*-type after irradiation and that the irradiation fluence is expected to be too low to significantly alter the mobility of the charge carriers. Thus, the HVPE samples qualitatively reproduce the observations in the bulk samples but without the presence of the E2 level. Conclusively, E2* seems to be formed by the irradiation but requiring also a thermally activated process to appear. The generation of E4* and E2* also takes place in MBE material, similar to that shown above for bulk and HVPE material, but the quantification is complicated by the presence of other deep levels.³⁶

Figure 9(a) shows a comparison of the DLTS spectra around the E2* level after several temperature cycles in bulk and HVPE material, as well as in two MBE samples. As stated above, the E2 concentration varies between samples and independent of the irradiation dose, consistent with an extrinsic impurity. On the other hand, E2* responds to the irradiation and the E2* concentration versus dose is shown in Fig. 9(b), accounting also for the influence of the λ -region. Indeed, a close to linear dose dependence is observed. The thermally

activated formation of a larger E2* concentration after the irradiation (Figs. 7 and 8) suggests two possibilities: either the formation of a defect complex or an activated rearrangement of the defect as may be possible with the V_{Ga} configurations at these temperatures.^{8,31}

For the former, we have already highlighted how H_i impurities are mobile at room temperature and it has been shown that they strongly interact with intrinsic defects such as vacancies.^{31,35} However, we find the electronic states calculated for these complexes to generally be located far deeper in the bandgap than the levels measured in Table I, which we also include in Table II. For example, our results suggest that the $\epsilon(0/-)$ associated with the highly stable V_{Ga}^{ib}-2H identified in Ref. 35 and shown in Fig. 6 falls \sim 1.3-1.5 eV above the VBM (\sim 3.4-3.6 eV below the CBM) and is not expected to contribute to the observed DLTS levels. Therefore, future measurements that probe the entire bandgap via traditional DLTS and optically assisted DLTS (DLOS) are necessary to further elucidate the defect kinetics and the correlation of various defect levels in as-grown and irradiated samples.

From the limited set of calculated defects summarized in Table II, we can come up with the following possible assignments for the E4* and E2* irradiation-induced levels in the absence of additional information. The first is that the E4* and E2* levels are associated with an isolated V_{Ga}, which through annealing leads to subsequent trapping of the vacancy in different configurations. From Fig. 5, the V_{Ga}^{ic} is predicted to be the most favorable in *n*-type conditions, with $\epsilon(-2/-3)$ at least 1.5 eV below the CBM, possibly consistent with the E4*.

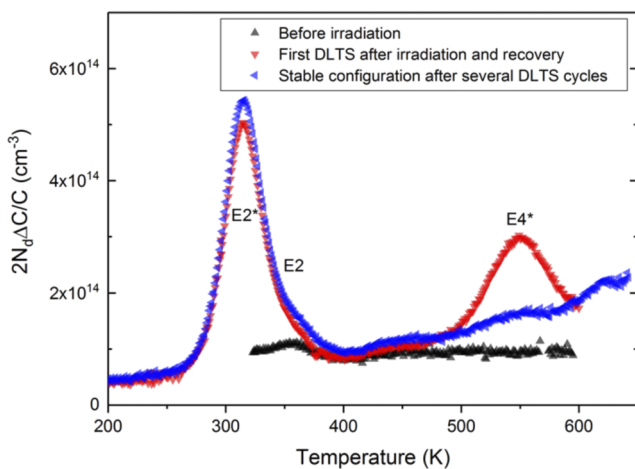
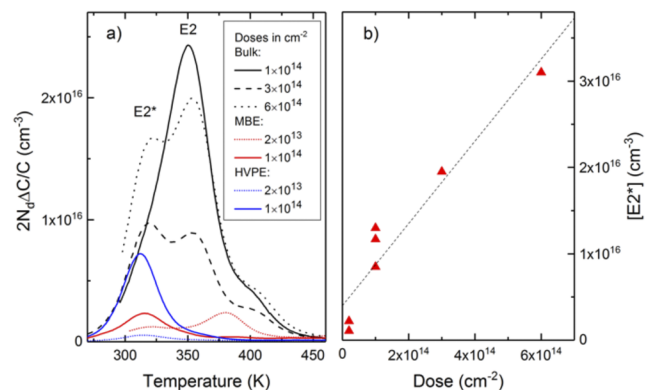
**FIG. 8.** DLTS measurements similar to Fig. 7 but on an HVPE sample before and after 2×10^{13} cm⁻² H⁺ irradiation. An increase in E2* is observed after several DLTS cycles, while E4* is quenched after the initial measurements.**FIG. 9.** (a) DLTS spectra illustrating the dose dependence of E2* for bulk and epitaxial samples. In (b), E2* concentration is extracted from (a), accounting also for the λ -region, and presented as function of dose. These data are after several cycles, i.e., in the stable configuration discussed in relation to Figs. 7 and 8.

TABLE II. Calculated energy level positions most relevant for comparison with the DLTS signals, shown relative to the conduction band edge ($E_c - E_t$) for comparison with the results in Table I. Values relative to the valence band edge can be found by adding the bandgap energy of 4.85 eV. The values are corrected for spurious finite-size effects in the periodic supercell assuming dielectric screening adopts ionic and electronic contributions (ϵ_0) and only electronic contributions (ϵ_∞), which give probable bounds for the levels most relevant for comparison with the experiment. Indented values denote adiabatic charge-state transition levels that are not thermodynamically stable (e.g., for negative-U defects) but that may be probed by DLTS measurements.

Defect level	Corrected with ϵ_0	Corrected with ϵ_∞
Ga _i (3+/2+)	-0.08	-1.40
Ga _i (2+/+)	-1.12	-1.52
Ga _i (3+/+)	-0.60	-1.46
Ga _{OI} (3+/+)	-0.93	-1.71
Ga _{OI} (3+/2+)	-0.83	-1.83
Ga _{OI} (2+/+)	-1.03	-1.60
Ga _{OI} (+/0)	+0.01	-0.28
Ga _{OII} (3+/+)	-1.03	-1.83
Ga _{OII} (3+/2+)	-0.95	-1.91
Ga _{OII} (2+/+)	-1.11	-1.75
Ga _{OII} (+/0)	-0.55	-0.76
Ga _{OII} (0/-1)	-0.25	-0.06
Ga _{OIII} (3+/+)	-1.06	-1.92
Ga _{OIII} (3+/2+)	-0.69	-1.73
Ga _{OIII} (2+/+)	-1.43	-2.11
O _{si} (+/0)	-3.26	-3.51
O _i (-1/-2)	-1.23	-0.64
V _{OI} (2+/0)	-1.50(-1.71 ^a)	-1.93(-2.10 ^a)
V _{OI} (2+/+)	-1.30	-1.94
V _{OI} (+/0)	-1.69	-1.91
V _{OII} (2+/0)	-2.23(-2.29 ^a)	-2.65(-2.68 ^a)
V _{OII} (2+/+)	-2.00	-2.64
V _{OII} (+/0)	-2.45	-2.66
V _{OIII} (2+/0)	-1.36(-1.56 ^a)	-1.79(-1.95 ^a)
V _{OIII} (2+/+)	-1.14	-1.78
V _{OIII} (+/0)	-1.68	-1.92
V _{GaI} (-2/-3)	-1.76(-1.64 ^a)	-0.69(-0.67 ^a)
V _{GaI} (-1/-2)	-2.32	-1.68
V _{GaII} (-2/-3)	-2.17(-2.12 ^a)	-1.11(-1.16 ^a)
V _{GaII} (-1/-2)	-2.50	-1.85
V _{Ga} ^{ia} (-2/-3)	-2.16	-1.07
V _{Ga} ^{ia} (-1/-2)	-2.39	-1.74
V _{Ga} ^{ia} (0/-1)	-3.16	-2.94
V _{Ga} ^{ib} (-2/-3)	-1.91	-0.87
V _{Ga} ^{ib} (-1/-2)	-2.11	-1.55
V _{Ga} ^{ib} (0/-1)	-3.29	-3.08
V _{Ga} ^{ic} (-2/-3)	-2.55	-1.50
V _{Ga} ^{ic} (-1/-2)	-2.82	-2.16
V _{Ga} ^{ic} (0/-1)	-3.23	-3.02
V _{Ga} ^{ib} -2H(0/-1)	-3.57	-3.35
V _{Ga} ^{ib} -2H(+0)	-4.12	-4.34
V _{Ga} ^{ic} -2H(0/-1)	-3.44	-3.26
V _{Ga} ^{ic} -2H(+0)	-4.18	-4.39
V _{Ga} ^{ia} -2H(0/-1)	-2.83	-2.61
V _{Ga} ^{ia} -V _{OII} (+/0)	-3.18	-3.39
V _{Ga} ^{ia} -V _{OII} (0/-1)	-2.84	-2.64
V _{Ga} ^{ia} -V _{OII} (-1/-3)	-1.16	-0.36
V _{Ga} ^{ia} -V _{OII} (-1/-2)	-0.84	-0.19
V _{Ga} ^{ia} -V _{OII} (-2/-3)	-1.49	-0.52
V _{Ga} ^{ib} -V _{OIII} (+/0)	-3.49	-3.70
V _{Ga} ^{ib} -V _{OIII} (0/-1)	-3.02	-2.80

TABLE II. (Continued.)

Defect level	Corrected with ϵ_0	Corrected with ϵ_∞
V _{Ga} ^{ic} -V _{OI} (+/0)	-3.50	-3.71
V _{Ga} ^{ic} -V _{OI} (0/-1)	-2.38	-2.16
V _{Ga} ^{ia} -2V _{OII} (+/0)	-1.02	-1.29
V _{Ga} ^{ia} -2V _{OII} (0/-2)	-1.02	-1.29
V _{Ga} ^{ia} -2V _{OII} (0/-)	-0.57	-0.41
V _{Ga} ^{ia} -2V _{OII} (-1/-2)	-0.95	-0.29
V _{Ga} ^{ia} -2V _{OII} (-2/-3)	-0.50	+0.41

^aComparisons with previous theory calculations from Ref. 6 are included.

The V_{Ga}^{ib} and less favorable V_{GaI} configurations also have $\epsilon(-2/-3)$ of at least ~ 0.7 eV,⁶ suggesting possible candidates for E2*. The main problems with an assignment of V_{Ga}^{ic} as E4* and V_{Ga}^{ib} as E2* are that (1) the V_{Ga}^{ic} is theoretically predicted to be thermodynamically and kinetically more stable than the V_{Ga}^{ib} in n-type conditions and (2) additional defect states within the DLTS window associated with V_{Ga}^{ib} like the $\epsilon(-1/-2) \sim 1.5$ eV below the CBM would also presumably increase if it were E2*. Both these points appear inconsistent with the measured DLTS signals and their evolution as seen from Figs. 7 and 8 and raises doubt that the E2* and E4* are associated with isolated V_{Ga}.

An additional interpretation is that the E4* level is associated with a Ga_i-derived signal, which through annealing leads to subsequent trapping at V_O that could lead to an increased E2* signal coming from Ga_O. The E4* would then effectively be a measurement of the Ga_i $\epsilon(2+/+)$ emission at $\sim E_c - 1.5$ eV, and the E2* would derive from the Ga_{OII} $\epsilon(+0)$ emission at $\sim E_c - 0.7$ eV, again assuming that only electronic screening is adequately captured in the calculations (the ϵ_∞ column in Table II). This explanation is hard to reconcile with the relatively low migration barrier calculated for Ga_i⁺, which would presumably diffuse at far lower temperatures than those probed during the DLTS scans. However, the Ga_{OII} and possibly other Ga_O configurations remain plausible candidates for the E2* level and should be investigated further.

Nonetheless, the dose dependence in Fig. 9 is an argument for E2* being a complex where at least one of the constituents is of an intrinsic origin generated by the irradiation, while Figs. 7 and 8 demonstrated that the complex formation is triggered by the heat treatment during the subsequent DLTS measurements. As previously mentioned, V_{Ga} and V_{OI} are reported to have a migration barrier of ≥ 0.7 and ≥ 1.7 eV, respectively.⁸ Hence, during annealing, one cannot rule out migration of V_O and the formation of V_{Ga}-V_O complexes beyond the few shown in Fig. 6. The V_{Ga}^{ia}-V_{OII} is one candidate complex with a $\epsilon(-2/-3)$ that falls within the range of E4*, with shifts in the levels associated with trapping another V_O in line with the E2*. Owing to the complexity of site symmetries and V_{Ga}ⁱ configurations, there are a wealth of possible combinations that can yield a rich array of defect levels within the bandgap that may be responsible

for the observed signals. Therefore, studying intrinsic defect complexes is a critical next step in clarifying the origins of the irradiation-induced defect levels in Ga_2O_3 .

While it has been claimed that $\beta\text{-Ga}_2\text{O}_3$ is a material with high radiation hardness, our present work indicates that there is substantial defect generation from collision damage produced by proton irradiation. Our study shows that complete charge carrier compensation occurs for relatively low irradiation doses, implying little dynamic annealing of the generated defects. However, the further observations show that we can recover most of the charge carriers with relatively low temperature annealing. Hybrid functional calculations suggest that the origin of the carrier depletion is due to Fermi level pinning from V_{Ga} acceptors and Ga_i and Ga_O donor species at least ~ 0.5 eV below the CBM. Carrier recovery is predicted to be mediated by V_{Ga} complex formation and passivation via H- or V_O -related defects. With reestablished concentrations of charge carriers after annealing, DLTS measurements showed that generation of two deep levels occur in the process. Of these, $\text{E}2^*$ appears to be activated by the annealing after irradiation, while a quenching of the $\text{E}4^*$ level concentration with annealing allows us to observe it only in the very first measurements after recovery. While we could not confirm the identities of the defects in this work using the tabulated defect levels for several candidate defects, evidence suggests that the $\text{E}2^*$ level is not an isolated V_{Ga} but likely a complex or possibly even a Ga_O . Future experimental and theoretical work is needed to better correlate the irradiation-induced defect levels like $\text{E}2^*$ and $\text{E}4^*$ with other levels across the entire bandgap to identify the defect(s) responsible.

See [supplementary material](#) for additional details on the calculations and formation energy plots from the manuscript obtained for the limits of electronic-only or electronic and ionic screening contributions to the finite-size corrections.

This work was partially performed under the auspices of the U.S. DOE by Lawrence Livermore National Laboratory under Contract No. DE-AC52-07NA27344 and supported by the Critical Materials Institute, an Energy Innovation Hub funded by the U.S. DOE, Office of Energy Efficiency and Renewable Energy, Advanced Manufacturing Office. The Research Council of Norway is acknowledged for the support to the Norwegian Micro- and Nano-Fabrication Facility, NorFab, Project No. 245963/F50.

REFERENCES

- ¹H. H. Tippins, *Phys. Rev.* **140**, A316 (1965).
- ²C. Janowitz, V. Scherer, M. Mohamed, A. Krapf, H. Dwelk, R. Manzke, Z. Galazka, R. Uecker, K. Irmscher, R. Fornari *et al.*, *New J. Phys.* **13**, 085014 (2011).
- ³M. Higashiwaki, K. Sasaki, A. Kuramata, T. Masui, and S. Yamakoshi, *Phys. Status Solidi A* **211**, 21 (2014).
- ⁴K. Sasaki, A. Kuramata, T. Masui, E. G. Vllora, K. Shimamura, and S. Yamakoshi, *Appl. Phys. Express* **5**, 035502 (2012).
- ⁵J. B. Varley, J. R. Weber, A. Janotti, and C. G. Van de Walle, *Appl. Phys. Lett.* **97**, 142106 (2010).
- ⁶P. Deák, Q. D. Ho, F. Seemann, B. Aradi, M. Lorke, and T. Frauenheim, *Phys. Rev. B* **95**, 35 (2017).
- ⁷M. A. Blanco, M. Sahariah, H. Jiang, A. Costales, and R. Pandey, *Phys. Rev. B* **72**, 184103 (2005).
- ⁸A. Kyrtos, M. Matsubara, and E. Bellotti, *Phys. Rev. B* **95**, 245202 (2017).
- ⁹K. Irmscher, Z. Galazka, M. Pietsch, R. Uecker, and R. Fornari, *J. Appl. Phys.* **110**, 063720 (2011).
- ¹⁰Z. Zhang, E. Farzana, A. R. Arehart, and S. A. Ringel, *Appl. Phys. Lett.* **108**, 052105 (2016).
- ¹¹M. E. Ingebrigtsen, L. Vines, G. Alfieri, A. Mihaila, U. Badstübner, B. G. Svensson, and A. Kuznetsov, *Silicon Carbide and Related Materials 2016*, Materials Science Forum Vol. 897 (Trans Tech Publications, 2017), pp. 755–758.
- ¹²J. F. Mcglone, Z. Xia, Y. Zhang, C. Joishi, S. Lodha, S. Rajan, S. A. Ringel, and A. R. Arehart, *IEEE Electron Device Lett.* **39**, 1042 (2018).
- ¹³A. Y. Polyakov, N. B. Smirnov, I. V. Shchemerov, E. B. Yakimov, J. Yang, F. Ren, G. Yang, J. Kim, A. Kuramata, and S. J. Pearton, *Appl. Phys. Lett.* **112**, 032107 (2018).
- ¹⁴J. F. Ziegler, M. Ziegler, and J. Biersack, in *19th International Conference on Ion Beam Analysis [Nucl. Instrum. Methods Phys. Res., Sect. B* **268**, 1818 (2010)].
- ¹⁵B. G. Svensson, K. Rydn, and B. M. S. Lewerentz, *J. Appl. Phys.* **66**, 1699 (1989).
- ¹⁶J. Heyd, G. E. Scuseria, and M. Ernzerhof, *J. Chem. Phys.* **118**, 8207 (2003).
- ¹⁷P. E. Blöchl, *Phys. Rev. B* **50**, 17953 (1994).
- ¹⁸G. Kresse and J. Furthmüller, *Phys. Rev. B* **54**, 11169 (1996).
- ¹⁹M. E. Ingebrigtsen, J. B. Varley, A. Y. Kuznetsov, B. G. Svensson, G. Alfieri, A. Mihaila, U. Badstübner, and L. Vines, *Appl. Phys. Lett.* **112**, 042104 (2018).
- ²⁰C. Freysoldt, J. Neugebauer, and C. G. Van de Walle, *Phys. Rev. Lett.* **102**, 016402 (2009).
- ²¹C. Freysoldt, B. Grabowski, T. Hickel, J. Neugebauer, G. Kresse, A. Janotti, and C. G. Van de Walle, *Rev. Mod. Phys.* **86**, 253 (2014).
- ²²Y. Kumagai and F. Oba, *Phys. Rev. B* **89**, 5 (2014).
- ²³M. Schubert, R. Korlacki, S. Knight, T. Hofmann, S. Schoeche, V. Darakchieva, E. Janzén, B. Monemar, D. Gogova, Q. T. Thieu *et al.*, *Phys. Rev. B* **93**, 125209 (2016).
- ²⁴J. J. Loferski and P. Rappaport, *Phys. Rev.* **111**, 432 (1958).
- ²⁵B. G. Svensson, C. Jagadish, A. Hallén, and J. Lalita, *Phys. Rev. B* **55**, 10498 (1997).
- ²⁶L. Vines, C. Bhoochoo, H. von Wenckstern, and M. Grundmann, *J. Phys.: Condens. Matter* **30**, 025502 (2018).
- ²⁷J.-M. Philibert, *Atom Movements-Diffusion and Mass Transport in Solids* (EDP Sciences, 2012).
- ²⁸C. Baban, Y. Toyoda, and M. Ogita, *J. Optoelectron. Adv. Mater.* **7**, 891 (2005).
- ²⁹G. Henkelman, B. P. Uberuaga, and H. Jónsson, *J. Chem. Phys.* **113**, 9901 (2000).
- ³⁰G. I. Csonka, J. P. Perdew, A. Ruzsinszky, P. H. T. Philipsen, S. Lebègue, J. Paier, O. A. Vydrov, and J. G. Ángyán, *Phys. Rev. B* **79**, 155107 (2009).
- ³¹J. B. Varley, H. Peelaers, A. Janotti, and C. G. Van de Walle, *J. Phys.: Condens. Matter* **23**, 334212 (2011).
- ³²T. Zacherle, P. C. Schmidt, and M. Martin, *Phys. Rev. B* **87**, 235206 (2013).
- ³³B. G. Janesko and G. E. Scuseria, *J. Chem. Phys.* **128**, 244112 (2008).
- ³⁴S. Ahn, F. Ren, E. Patrick, M. E. Law, S. J. Pearton, and A. Kuramata, *Appl. Phys. Lett.* **109**, 242108 (2016).
- ³⁵P. Weiser, M. Stavola, W. B. Fowler, Y. Qin, and S. Pearton, *Appl. Phys. Lett.* **112**, 232104 (2018).
- ³⁶M. E. Ingebrigtsen, L. Vines, G. Alfieri, A. Mihaila, and A. K. U. Badstbner, “Generation and metastability of deep level states in $\beta\text{-Ga}_2\text{O}_3$ exposed to reverse bias at elevated temperatures” (unpublished).